Rainfall simulation and Structure-from-Motion photogrammetry for the analysis of soil water erosion in Mediterranean vineyards

Massimo Prosdocimi [a,*], Maria Burguet [b], Simone Di Prima [c], Giulia Sofia [a], Enric Terol [d], Jesús Rodrigo Comino [e,f], Artemi Cerdà [b,g], Paolo Tarolli [a]

[a] Department of Land, Environment, Agriculture and Forestry, University of Padova, Agripolis, Viale dell'Università 16, 35020 Legnaro, PD, Italy
[b] Soil Erosion and Degradation Research Group, Department of Geography, University of Valencia, Blasco Ibáñez, 28, 46010, Valencia, Spain
[c] Dipartimento di Agraria, Università degli Studi di Sassari, Viale Italia 39, 07100 Sassari, Italy
[d] Department of Cartographic Engineering, Geodesy and Photogrammetry, Universitat Politècnica de València, Camino de Vera, s/n, 46022 Valencia, Spain
[e] Physical Geography, Trier University, 54286 Trier, Germany
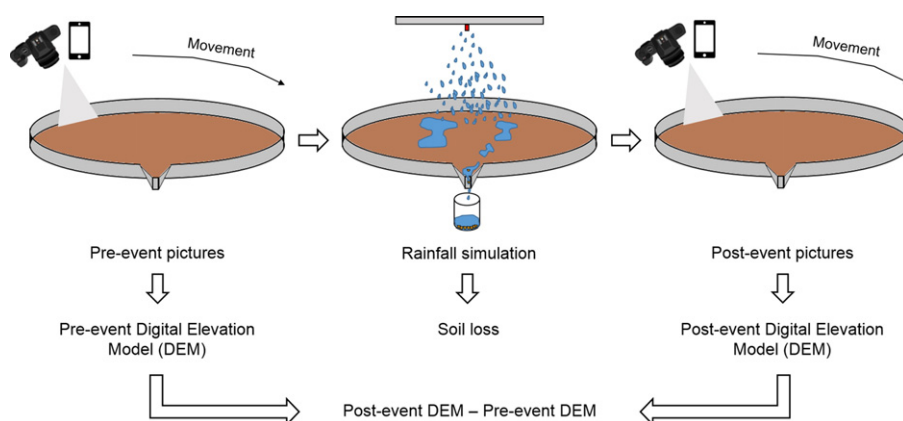[f] Instituto de Geomorfología y Suelos, University of Málaga, 29071 Málaga, Spain
[g] Soil Physics and Land Management Group, Wageningen University, Droevendaalsesteeg 4, 6708PB Wageningen, The Netherlands

HIGHLIGHTS

- Structure-from-Motion is able to detect topographic changes at very fine scales.
- Smartphones can be used to obtain reliable image datasets for Structure-from-Motion.
- Sediment connectivity plays a key role in estimating eroded materials.

GRAPHICAL ABSTRACT

ARTICLE INFO

ABSTRACT

Soil water erosion is a serious problem, especially in agricultural lands. Among these, vineyards deserve attention, because they constitute for the Mediterranean areas a type of land use affected by high soil losses. A significant problem related to the study of soil water erosion in these areas consists in the lack of a standardized procedure of collecting data and reporting results, mainly due to a variability among the measurement methods applied. Given this issue and the seriousness of soil water erosion in Mediterranean vineyards, this works aims to quantify the soil losses caused by simulated rainstorms, and compare them with each other depending on two different methodologies: (i) rainfall simulation and (ii) surface elevation change-based, relying on high-resolution Digital Elevation Models (DEMs) derived from a photogrammetric technique (Structure-from-Motion or SfM). The experiments were carried out in a typical Mediterranean vineyard, located in eastern Spain, at very fine scales. SfM data were obtained from one reflex camera and a smartphone built-in camera. An index of sediment connectivity was also applied to evaluate the potential effect of connectivity within the plots. DEMs derived from the smartphone and the reflex camera were comparable with each other in terms of accuracy and capability of estimating soil loss. Furthermore, soil loss estimated with the surface elevation change-based method resulted to be

* Corresponding author.
  E-mail addresses: massimo.prosdocimi@studenti.unipd.it (M. Prosdocimi), artemio.cerda@uv.es, artemio.cerdabolinches@wur.nl (A. Cerdà).

of the same order of magnitude of that one obtained with rainfall simulation, as long as the sediment connectivity within the plot was considered. High-resolution topography derived from SfM revealed to be essential in the sediment connectivity analysis and, therefore, in the estimation of eroded materials, when comparing them to those derived from the rainfall simulation methodology. The fact that smartphones built-in cameras could produce as much satisfying results as those derived from reflex cameras is a high value added for using SfM.

1. Introduction

Throughout the world, soil erosion by water is a serious problem, especially in semi-arid and semi-humid areas (Cerdà et al., 2009, 2015; Cerdan et al., 2010; Garcìa-Ruiz, 2010; Ligonja and Shrestha, 2015; Novara et al., 2016;Taguas et al., 2015; Rodrigo Comino et al., 2016a). Although soil erosion by water consists of physical processes that vary significantly in severity and frequency according to when and where they occur, they are also strongly influenced by anthropic factors such as land-use changes on large scales and unsustainable farming practices (Cerdà, 2000; León et al., 2015; López-Vicente et al., 2015; Ochoa-Cueva et al., 2015; Montgomery, 2007; Mwango et al., 2016; Nanko et al., 2015; Tarolli et al., 2014). This has led to the definition of 'accelerated' soil erosion as being the result of human impact on the landscape (Tarolli and Sofia, 2016) and this is found in all the continents (Borrelli et al., 2015; Cao et al., 2015; Gessesse et al., 2015; Rodrigo Comino et al., 2016b).

The impact of soil erosion on modern society has required to set threshold values against which to assess the monitoring of soil data, especially in agriculture (Montgomery, 2007). Among the cultivated lands, vineyards merit a particular attention, because, aside from representing one of the most important crops in terms of income and employment, they also constitute, for the Mediterranean areas, a form of agricultural land use that causes the highest soil losses (Cerdà and Doerr, 2007; Cerdan et al., 2010; Martínez-Casasnovas and Sánchez-Bosch, 2000; Prosdocimi et al., 2016a; Raclot et al., 2009; Rodrigo Comino et al., 2015; Rodrigo Comino et al., 2016c). One of the main reasons for this is the bare soil under the vines that is exposed to high intensity rainfall events, mainly concentrated in spring, autumn and winter, which characterize the Mediterranean climate (Arnáez et al., 2007; Borga et al., 2011; Garcìa-Ruiz, 2010; Prosdocimi et al., 2016a). For this cultivation, the two most common soil management techniques are considered to be tillage, where the weeds are usually removed mechanically, and no-tillage, where the weeds are usually removed chemically (Novara et al., 2011; Raclot et al., 2009), and both of them generally turn out in bare soil management during the whole year. Extreme rainfall events that occur in the Mediterranean area are able to cause significant soil water erosion processes, especially when no protective material covers the soil (Fig. 1) (Bisantino et al., 2015; Keesstra et al., 2016; Novara et al., 2016;

Prosdocimi et al., 2016c). However, to reduce the high soil erosion rates, more conservation-minded soil management practices have also been used such as mulching (Cerdà et al., 2015; Costantini et al., 2015; Jordán et al., 2011; Prosdocimi et al., 2016b, 2016c), cover crops (Novara et al., 2011), rock fragments (Blavet et al., 2009), natural grassing (Grimaldi et al., 2015; Mekonnen et al., 2015a; Mekuria et al., 2016; Raclot et al., 2009) and geotextiles (Giménez Morera et al., 2010; Mekonnen et al., 2015b; Mengistu et al., 2016). Furthermore, new approaches to evaluate incentives for the adoption of agri-environment measures in degraded and eroded vineyards have been implemented (Galati et al., 2015) and mulching is one of those successful strategies (Prosdocimi et al., 2016c).

Another issue related to soil water erosion in Mediterranean vineyards is the lack of a standardized procedure of collecting data and reporting results, mainly due to a great variability among the measurement methods applied to quantify it (Prosdocimi et al., 2016a; García-Ruiz et al., 2015). This induces difficulties in comparing data coming from different studies and obtained with different methodologies. Based on the paper review of Prosdocimi et al. (2016a), six different methodologies to assess soil water erosion in vineyards have been identified: (i) experimental plot stations under simulated or natural rainfalls, (ii) erosion markers, (iii) models, (iv) the surface elevation change-based methods, (v) geochemical methods, and (vi) carbon stable isotopes. This works focuses on the use of plot stations under simulated rainfall and on the surface elevation change-based method. Rainfall simulation has become a very effective technique for assessing soil erosion, particle detachment and overland flow at very fine scales (Arnáez et al., 2007; Cerdà et al., 1997; Iserloh et al., 2013; Rodrigo Comino et al., 2016b). Several types and designs of rainfall simulators have been realized to meet the objectives of researchers (Iserloh et al., 2013; Lassu et al., 2015). In particular, the advantages of using a portable rainfall simulator are: i) its versatility, ii) low cost and easy operation, and iii) capability of obtaining data under controlled conditions and over relatively short periods of time. The surface elevation change-based method is able to detect the topographic changes over time. It relies on Digital Elevation Models (DEMs) that can be used as basic topographic information to derive morphometric attributes and quantify soil erosion and deposition rates (Martínez-Casasnovas and Sánchez-Bosch, 2000; Martínez-Casasnovas et al., 2002; Prosdocimi et al., 2015). Remote-sensing technologies have proven to facilitate significantly the
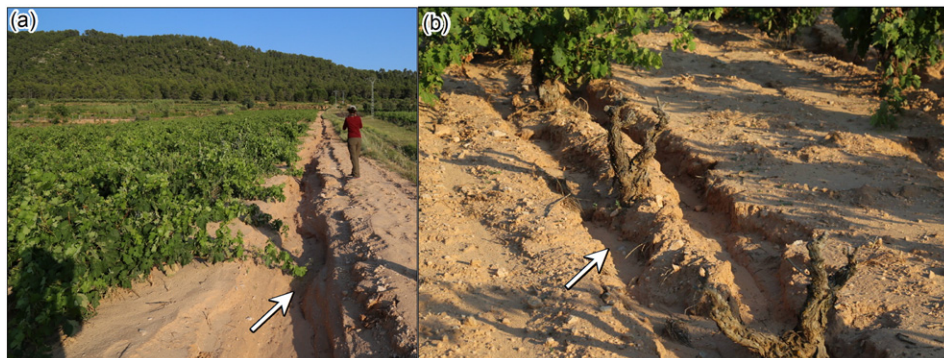

Fig. 1. Examples of soil water erosion processes caused by a 40 mm in 30 min thunderstorm occurred in mid-June 2015 in the study area. The white arrows point out a gully (a) and a rill (b).

creation of high-resolution DEMs (Aucelli et al., 2016; Tarolli, 2014; Tarolli et al., 2015), and the availability of DEMs at multiple scales in terms of resolution but also temporal coverage is becoming essential to the understanding of global issues, such sediment production and anthropogenic changes to the Earth system, among others (Sofia et al., 2016). The recent development of the photogrammetric technique 'Structure-from-Motion' (SfM) has confirmed to represent a valid and cheaper alternative to the established airborne and terrestrial lidar (Light Detection and Ranging) technology for measuring soil surface changes in different environments (Dandois and Ellis, 2013; Eltner et al., 2015; James and Robson, 2012; Masiero et al., 2015; Piermattei et al., 2016; Westoby et al., 2012; Whitehead et al., 2013; Woodget et al., 2015). All this information can shed light into the connectivity within the soil and water losses (López-Vicente et al., 2016; Marchamalo et al., 2016; Masselink et al., 2016).

The growing interest for SfM has been enhanced by the fact that it is a user-friendly technique, and that it can also rely on smartphone built-in cameras (Masiero and Vettore, 2016; Micheletti et al., 2014; Prosdocimi et al., 2015) and on the diffusion of unmanned aerial vehicles (UAVs) (Chen et al., 2015; Colomina and Molina, 2014).

Given the seriousness of soil water erosion in Mediterranean agricultural lands and the issue of putting data obtained with different methodologies in relation to each other, this works intends to quantify the soil losses caused by simulated rainstorms, and compare them with each other depending on two different methodologies used: (i) rainfall simulation and (ii) surface elevation change-based, relying on high-resolution DEMs derived from SfM. Furthermore, this work aims to compare the results obtained from SfM with each other, depending on the type of camera used. The objectives are pursued by carrying out the experiments in a typical Mediterranean vineyard, under tillage conditions, located within the province of Valencia (Spain), at very fine scales (0.25 m^2).

2. Material and methods

2.1. Study area

The study area consists in a 25-year-old vineyard, located at El Celler del Roure in Les Alcusses de Moixent, within the Canyoles river watershed in the province of Valencia (La Costera District, eastern Spain) (38° 48′ 33.12″ N, 0° 49′ 3.27″ O). Vines are located parallel to the contour lines and the inter-rows, which are about 2.5 m wide, are artificially maintained bare during the whole year through tillage operations carried out with a Landini Rex 95 tractor which adopts a tooth arrow as farm implement. The portion affected by the tractor wheel tracks results to be about 36% of the total inter-row area (Fig. 2). Climate is typically Mediterranean with 3–5 months of summer drought (June–September). Mean annual rainfall is about 350 mm yr^{-1}. Rainfall is distributed among autumn, winter and spring, with maximum peak rainfall intensities during the autumn season, where values higher of 200 mm day^{-1} were recorded during the last 50 years. Mean annual temperature is about 13.8 °C while the hottest month (August) has average temperatures of about 23 °C. The parent materials in this area belong to Cretaceous limestones and Tertiary Marly deposits that develop Typic Xerothent soils (Soil Survey Staff, 1998). The soils are characterized by low levels of soil organic matter (<1%) due to the millennia of agricultural use and soil disturbance (ploughing), basic pH (8) (Prosdocimi et al., 2016b), sandy loam soil textures (clay 19.3%, silt 13.4% and sand 67.3%), and low bulk density (1.109 g cm^{-3}).

To better characterize the climate of our study site, Walter-Lieth climate diagram (Walter and Lieth, 1960) has been obtained using data derived from Ontinyent climate station as it is the one with the longest records (29 years) closest to the study site (about 17 km) (Fig. 3). The diagram displays monthly averages for temperature and precipitation over a year. When the precipitation curve undercuts the temperature

Fig. 2. Visual perspective of the tilled inter-rows where the prostractor wheel tracks are well visible (black arrows) (a). The white arrows stress the soil sediments that were transported following the 40 mm in 30 min thunderstorm occurred in mid-June 2015.

curve, the area in between them indicates dry season. When the precipitation curve supersedes the temperature curve, the area in between them indicates moist season. For further information, readers may refer to http://www.globalbioclimatics.org/.

2.2. Experimental plot design

Four circular steel plots (0.25 m^2) were located in the bare inter-rows of the vines managed with conventional tillage, and are referred to in the text as 1, 2, 3 and 4. Each plot was placed in a different inter-row and had an outlet, which allowed to converge and collect the surface runoff samples during the runoff simulation experiments. For each plot, five targets (SfM-targets), made of black and white polythene squares, were used: four (5.5 cm × 5.5 cm) were placed outside the circular plots and one (2.5 cm × 2.5 cm) inside the plot (Fig. 4).

SfM-targets centroids were surveyed using a Topcon GRS-1 rover receiver running in real time kinematic (RTK) mode. In addition, other thirteen ground-control points (GCPs) were surveyed in the immediate neighborhood of each plot.

2.3. Rainfall simulation

A one-nozzle (Hardi-1553-12) rainfall simulator was used to reproduce seven rainstorms at 55 mm h^{-1} rainfall intensity for one hour on the 4 circular plots of 0.25 m^2. For plots 1, 2 and 3, a single rainfall experiment was carried out, while for plot 4, four rainfall experiments were carried out during four consecutive days, and are referred to in the text as 4A, 4B, 4C and 4D. Storms similar to the ones simulated have a return period of 10 years in the study area (Cerdà, 1996; Prosdocimi et al., 2016b). The rainfall simulator used was the one described by Cerdà et al. (1997) because it revealed to be effective in rugged terrain conditions proving to give good results in semi-arid environments. Its basic components are a nozzle, a structure that holds the nozzle, the connection with the water supply, the pumping system and a tarpaulin to protect the rainfall simulation from wind. As the nozzle was kept at about 2 m height over a plane surface, the 0.25 m^2 plots were established at the centre of the 1 m^2 sprinkling area, to avoid border interference. Readers are referred to Cerdà et al. (1997) and Iserloh et al. (2013) for a further description of the rainfall simulator used and Cerdà (1996, 1997) for more information about the distribution of
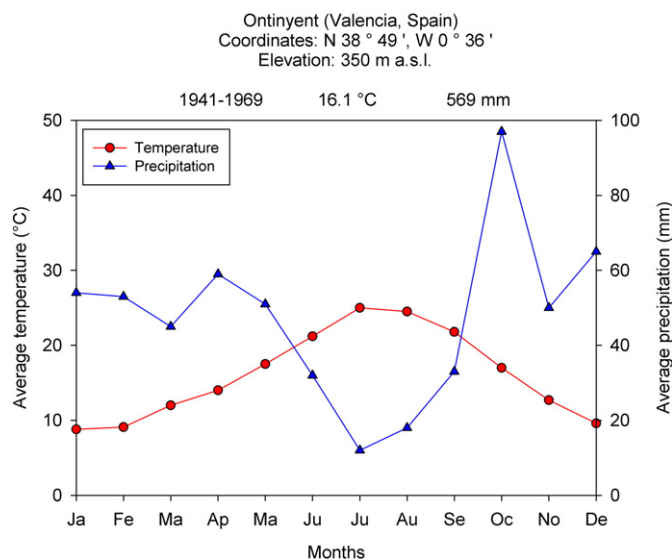
rainfall parameters. Surface runoff from the plots were collected and measured at 1-min intervals during each simulated rainfall event. Every tenth 1-min runoff sample was collected for laboratory analysis in order to determine sediment concentration, that was obtained after the desiccation of the samples in the laboratory. Then, runoff rates and sediment concentration were used to calculate the soil loss, runoff, runoff coefficient, and erosion rates.

2.4. Surface elevation changes through Structure-from-Motion

Photographs of each plot were taken using two different types of camera: (i) a standalone digital reflex camera (Nikon D3000 at 10.2 MP resolution, set at a focal length of 35 mm) and (ii) a smartphone, precisely a BQ Aquaris E5, built-in camera (13 MP resolution) with both automatic focusing and exposure enabled. The choice of using two cameras was due to test the effectiveness of SfM, also when it relies on an image dataset derived from a smartphone. Twenty photographs were taken before and after the rainfall simulation using each camera. A 1 m high support having two boxes, that were 0.3 m far from each other and capable of holding the cameras, was used to take the pictures (Fig. 5). Photographs were taken inside the rainfall simulator covered by the tarpaulin to have a homogeneous light over the plots.

The SfM technique was then used to obtain three-dimensional (3D) georeferenced point clouds and to generate 0.01 m resolution DEMs for each plot. The thirteen points collected in the immediate neighborhood of each plot (see the previous chapter Experimental plot design) were used as GCPs to assess the accuracy and precision of the DEMs through the computation of the root-mean-square-error (RMSE), mean error, and standard deviation of error (SDE). The working principles of SfM are similar to those of stereoscopic photogrammetry, namely that the 3D model can be created from overlapping, offset images. However, unlike traditional photogrammetry, in which either the position of the camera or the positions of some points are known prior to scene reconstruction (Fonstad et al., 2013; Verhoeven et al., 2012; Westoby et al., 2012), in the SfM, matches are made between points across many photographs without prior knowledge of the camera position (Lowe, 2004).

The images acquired were processed using the commercial software Agisoft PhotoScan®, as already successfully considered in different analyses (Doneus et al., 2011; Javernick et al., 2014; Piermattei et al., 2016; Prosdocimi et al., 2015; Verhoeven et al., 2012; Woodget et al., 2015). A custom algorithm similar to the Lowe's (2004) Scale Invariant Feature Transform (SIFT) object recognition system was used by the software to determine the 3D location of matching features in multiple images. Then, camera position was calculated by estimating the camera's intrinsic (focal length, principal point, and lens distortion) and extrinsic (projection centre location and the six exterior orientation parameters that define the image) orientation parameters. This was done by using a bundle-adjustment algorithm (Javernick et al., 2014; Robertson and Cipolla, 2009; Verhoeven et al., 2012). Afterwards, the software created a dense surface, usually referred to as mesh, by using these parameters and a dense multi-view stereo reconstruction (DMVR) (Agisoft, 2016). The mesh was generated in a relative 'image-space' coordinate system (Westoby et al., 2012), and therefore, it required to undergo a linear similarity transformation using seven parameters (three translation, three rotation, and one scaling), based on known GCPs, to be transformed to an absolute coordinate system. The GCPs corresponded to the SfM-targets centroids, whose x, y and z coordinates were previously recorded with Topcon GRS-1. As the linear similarity transformation could not remove non-linear model misalignments (Woodget et al., 2015), an optimization transformation method was applied to minimize geometric distortions within the mesh (Agisoft, 2016). Thereafter the mesh was rebuilt and the 3D georeferenced point could be exported. The georeferenced point clouds are referred to in the text as GEOPre$_{NKN}$ and GEOPost$_{NKN}$, for those derived from the Nikon camera before and after the rainfall simulation, respectively, and GEOPre$_{PHO}$ and GEOPost$_{PHO}$ for those derived from

Ontinyent (Valencia, Spain)
Coordinates: N 38 ° 49 ', W 0 ° 36 '
Elevation: 350 m a.s.l.

1941-1969   16.1 °C   569 mm

Fig. 3. Walter-Lieth climate diagram (Walter and Lieth, 1960) computed for the Ontinyent climate station as it is the one with the longest records (29 years) closest to our study site (about 17 km). The information above the panel corresponds to station location, the period of years recorded, the mean annual temperature and the mean annual precipitation.
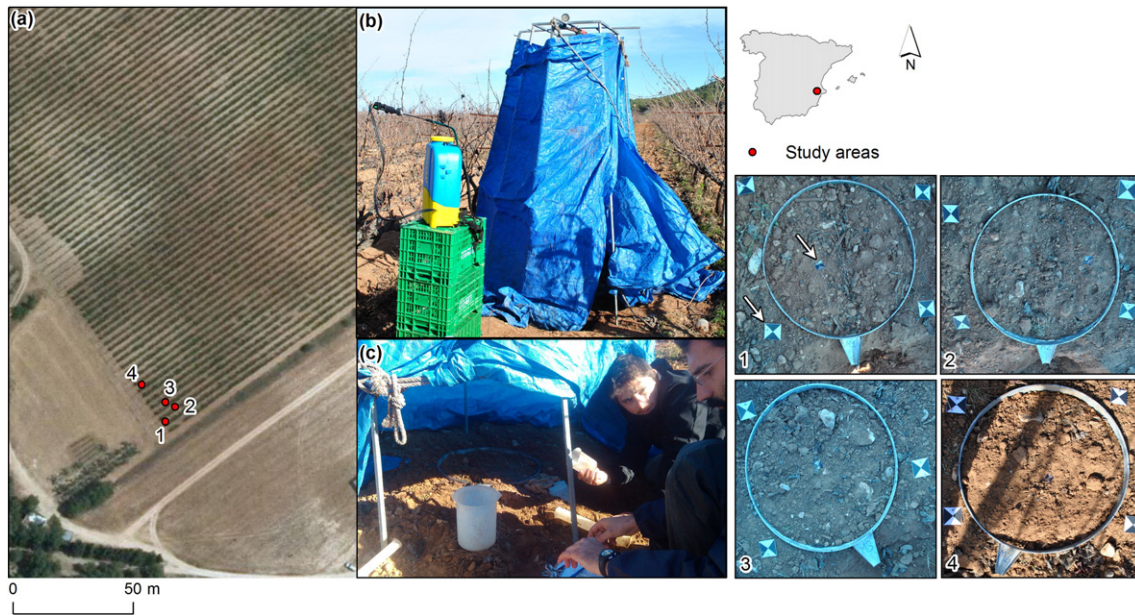
Fig. 4. Localization of the study areas (a), that correspond to the four circular plots (1, 2, 3 and 4) where the rainfall simulation and photogrammetric surveys were carried out. Views of the rainfall simulator (b) and of the rainfall simulation experiment in action (c) are also shown.

the smartphone camera before and after the rainfall simulation, respectively. Furthermore, the number of the plot is also included (1, 2, 3, 4A, 4B, 4C and 4D).

Then, the SfM final point clouds were further manipulated using the open source program CloudCompare® (Girardeau-Montaut, 2015) to remove additional noise that typically affects these data (Javernick et al., 2014; Prosdocimi et al., 2015). In this case, given the small size of the plots, the noise removal was accomplished manually. Finally, the elevation points were interpolated by the natural neighbor method (Sibson, 1981) to generate 0.01 m resolution DEMs. The DEMs are referred to in the text as DEMPre$_{NKN}$ and DEMPost$_{NKN}$, for those derived from the Nikon camera before and after the rainfall simulation, respectively, and DEMPre$_{PHO}$ and DEMPost$_{PHO}$ for those derived from the smartphone camera before and after the rainfall simulation, respectively. Furthermore, the number of the plot is also included (1, 2, 3, 4A, 4B, 4C and 4D). The DEMsPre$_{NKN}$ obtained for each plot are shown in Fig. 6.

For the objectives of this work, all the analysis was based on the final DEMs, as done by Bangen et al. (2014), Calligaro et al. (2013), Javernick et al. (2014), Prosdocimi et al. (2015), Tarolli et al. (2015), and Wechsler (2007). The DEMs derived from the smartphone were then directly compared to the DEMs derived from the camera, by assuming a normal distribution and using robust statistical methods (Höhle and Höhle, 2009; Prosdocimi et al., 2015). This entailed the computation of the mean error, SDE, RSME, median, and normalized median absolute deviation (NMAD).

2.5. Computation of soil loss

Soil loss was computed for both rainfall simulation and surface elevation change-based methodologies. For rainfall simulation methodology, the runoff samples were used to determine the sediment concentration and, then, the runoff rates and sediment concentration were used to
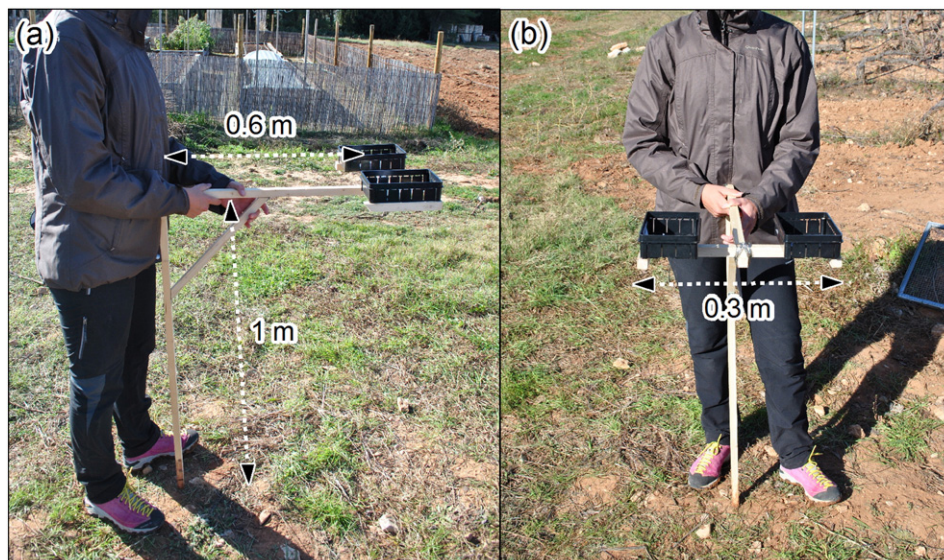
Fig. 5. Two visual perspectives of the support used to take the pictures. The support consists in a main pole, 1 m high, with two boxes that stick out the main pole for 0.6 m (a) and are 0.3 m far from each other (b). The boxes were designed to hold the cameras with the lens downwards facing.
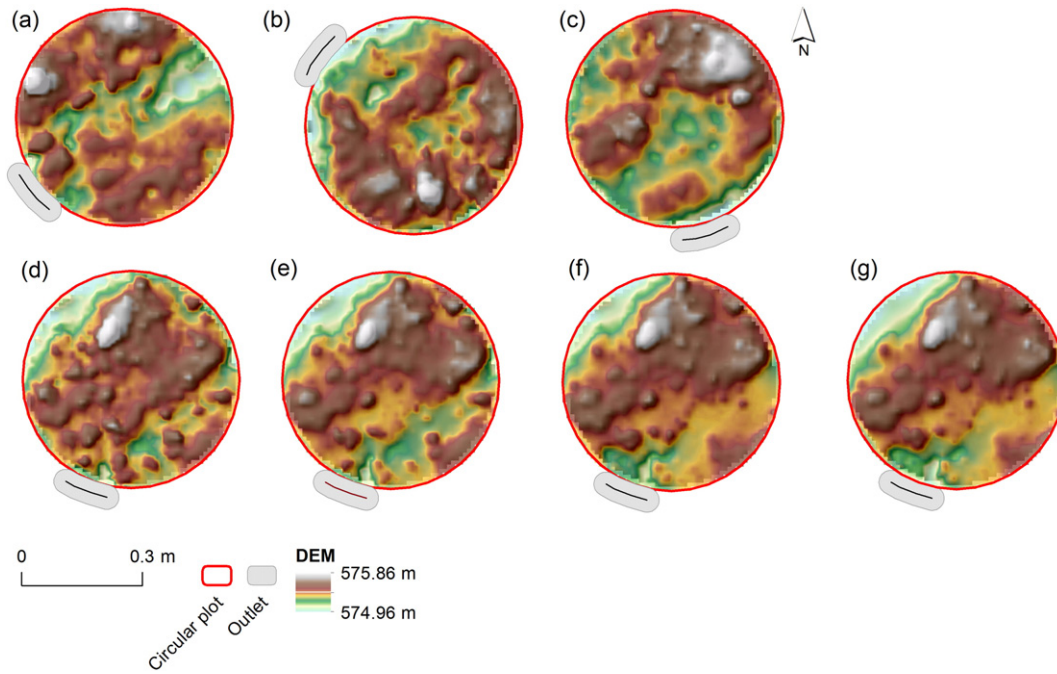
Fig. 6. DEMsPre$_{NKN}$ (0.01 m resolution) obtained for each plot: (a) DEMs1Pre$_{NKN}$, (b) DEMs2Pre$_{NKN}$, (c) DEMs3Pre$_{NKN}$, (d) DEMs4APre$_{NKN}$, (e) DEMs4BPre$_{NKN}$, (f) DEMs4CPre$_{NKN}$, and (g) DEMs4DPre$_{NKN}$.

calculate the total soil loss (g). For the surface elevation change-based methodology, SfM was applied to obtain high-resolution DEMs before (DEMsPre) and after (DEMsPost) the rainfall simulation. Then, the so-called morphological method (Ashmore and Church, 1998) was used to estimate the soil loss. The morphological method consists in carrying out repeated topographic surveys from which DEMs can be obtained and differenced to produce DEMs of difference (DoDs). The volumes of eroded materials (cm³) were computed by considering the DEMsPre and DEMsPost for each plot and for each camera by using the Geomorphic Change Detection (GCD) 6.1.14 toolbar embedded in an ESRI® add-in for ArcGIS 10.X that is freely downloadable from http://gcd.joewheaton.org/downloads. Then, the volumes of eroded materials were turned into soil loss expressed in grams, by knowing the bulk density. The GCD allows to compute the volumes of deposited materials too, but, for this work, only eroded materials have been considered, to make a comparison with the soil loss derived from the rainfall simulation methodology. The DoDs are referred to in the text as DoDs$_{NKN}$ and DoDs$_{PHO}$ for those derived from the Nikon and smartphone cameras, respectively. DEMs' uncertainty in DoDs has also been considered (Brasington et al., 2000; Lane et al., 1994; Lane, 1998; Lane et al., 2003; Prosdocimi et al., 2015; Wheaton, 2008; Wheaton et al., 2010). In this case, DEMs' uncertainties were evaluated according to a probabilistic thresholding that can be carried out with a user-defined confidence interval (Brasington et al., 2003; Lane et al., 2003; Taylor, 1997):

$$U_{crit} = t\left(\sqrt{SDE_{new}^2 + SDE_{old}^2}\right) \qquad (1)$$

where U_{crit} is the critical threshold error propagated in the DoD and SDE_{new} and SDE_{old} are the individual standard deviation errors in DEM$_{new}$ (post-event) and DEM$_{old}$ (pre-event), respectively. U_{crit} is based on a critical student's t-value at a chosen confidence interval where:

$$t = \frac{|z_{DEMnew} - z_{DEMold}|}{\delta u_{DoD}} \qquad (2)$$

where $|z_{DEMnew} - z_{DEMold}|$ is simply the absolute value of the DoD. The probability of a DoD predicted elevation change occurring due the

uncertainty can then be calculated by relating the t-statistic to its cumulative distribution function. In this work, we used the 95% confidence interval as a threshold, as also suggested by Wheaton et al. (2010).

2.6. Sediment connectivity

Sediment connectivity is defined as the connected transfer of sediment from a source to a sink in a system through processes of sediment detachment and transport (Bracken et al., 2015). The concept of connectivity has increasingly been used in quantitative process-based sediment dynamics research, especially at catchment scales (Ali et al., 2014; Baartman et al., 2013; Bracken and Croke, 2007; Bracken et al., 2015; Brierley et al., 2006; Cavalli et al., 2013; Fryirs et al., 2007; Heckmann and Schwanghart, 2013; Lexartza-Artza and Wainwright, 2011; López-Vicente et al., 2013; Wainwright et al., 2011). Geomorphology has been considered as a major driver on determining sediment connectivity (Heckmann and Schwanghart, 2013; Theler et al., 2010), and geomorphometric indices have increasingly been developed to assess it (Borselli et al., 2008; Cavalli et al., 2013; López-Vicente et al., 2013; Reid et al., 2007; Sougnez et al., 2011). In this study we applied the index of connectivity (IC) as proposed by Cavalli et al. (2013) based on the work of Borselli et al. (2008), to evaluate the potential effect of sediment connectivity within the plots. The reasons for this choice relied on the facts that the IC (i) is a distributed geomorphometric index that can be easily derived from a DEM, (ii) can be computed with reference to specific target features, and (iii) has been adapted for high-resolution DEMs. The IC has been developed as a ToolBox for ArcGis 10.1 or as stand-alone application based on Python scripting with bindings for processing geographical datasets. It uses functionalities and algorithms available in TauDEM 5.2 tool (Tarboton, 2013) and it is freely downloadable from http://www.sedalp.eu/download/tools.shtml. This index mainly focuses on the influence of topography on sediment connectivity, and takes into account the characteristics of the drainage area (upslope component, D_{up}) and the flow path length that a particle has to travel to arrive at the nearest sink (downslope component, D_{dn}).

The IC is computed as follows:

$$IC = \log_{10}\left(\frac{D_{up}}{D_{dn}}\right) = \log_{10}\left(\frac{\overline{WS}\sqrt{A}}{\sum_i \frac{d_i}{W_i S_i}}\right) \tag{3}$$

where $\overline{W}$ is the average weighting factor of the upslope contributing area (dimensionless), $\overline{S}$ is the average slope gradient of the upslope contributing area (m/m), A is the upslope contributing area (m^2), d_i is the length of the flow path along the ith cell according to the steepest downslope direction (m), W_i and S_i are the weighting factor and the slope gradient of the ith cell, respectively. IC can assume values ranging from -∞ to +∞, with connectivity increasing for larger IC values.

3. Results and discussion

3.1. Nikon and smartphone built-in cameras comparisons

Regarding the comparisons between the Nikon and smartphone built-in cameras, the georeferentiation errors (RMSE) calculated by the Agisoft PhotoScan® software along the x, y and z-axes for each SfM point cloud are reported (Table 1). The SfM point clouds show an average error of the order of about 0.01 m along the x-axis, and an even lower order error along the y and z-axes. These good results support the choice of setting the DEMs resolution equal to 0.01 m and can be explained by the fact that: (i) the plots were very small, (ii) the 5 SfM-targets were well distributed over each plot, and (iii) the pictures were taken in a correct way, thanks to the support used, the expedient of shooting photographs inside the tarpaulin, and the short distance between the position of the cameras and the plots (about 1 m). Furthermore, differences between the DEMs$_{PHO}$ and DEMs$_{NKN}$ for the unthresholded DEMs (where no uncertainty analysis was carried out) were also evaluated with accuracy measures assuming a normal distribution and more robust parameters too (Table 2). From Table 2, emerges that all the DEMs$_{PHO}$ are comparable to DEMs$_{NKN}$. Mean values are of the order of about 0.0001 m and SDE values of the order of about 0.001 m. Skewness and kurtosis confirm the fact that the elevation differences do not follow normal distributions (Höhle and Höhle, 2009; Sofia et al., 2013), and this supports the choice of considering more robust parameters too such as NMAD and median. However, also when considering these more robust approaches, DEMs$_{PHO}$ confirm to be comparable to DEMs$_{NKN}$, showing NMAD and median values of the order of about 0.001 and 0.001 m, respectively.

3.2. Soil loss

Fig. 7 shows the DoDs derived from SfM, by considering the DEMsPre$_{NKN}$ and DEMsPost$_{NKN}$ for each plot, thresholded according to the probabilistic thresholding with a 95% confidence interval. The fact that, the thresholding of DoDs entails a loss of information, is expected and occurs at the expense of a better geomorphic plausibility (Wheaton et al., 2010). Elevation differences range from negative values (red colour), to which correspond net eroded sediments, to positive values (blue colour), to which correspond net deposited sediments. From Fig. 7 emerges that plots 1, 2, 3 and 4A mainly show negative elevation differences. This means that the single simulated rainfall event caused more erosion than deposition, and this can be explained by the fact that the plots, at the beginning, have more material which is prone to be washed away. In contrast, plots 4B, 4C and 4D show greater elevation differences. This suggests that, as rainfall events follow one another, the soil particles, that are susceptible to be eroded, diminish, and therefore, the soil shows elevation differences which are closer to zero values, where zero corresponds exactly to no difference at all between before and after the rainstorm.

Table 1
Georeferentiation errors (RMSE) calculated by Agisoft PhotoScan® along the x, y and z-axes for each point cloud derived from SfM technique. GEOPre$_{NKN}$ and GEOPost$_{NKN}$ refer to the point clouds derived from the Nikon camera before and after the rainfall simulation, respectively, and GEOPre$_{PHO}$ and GEOPost$_{PHO}$ for those derived from the smartphone camera before and after the rainfall simulation, respectively. The number of the plot is also included (1, 2, 3, 4A, 4B, 4C and 4D).

	X Error ($\pm$m)	Y Error ($\pm$m)	Z Error ($\pm$m)
GEO1Pre$_{NKN}$	0.0119	0.0030	0.0038
GEO1Pre$_{PHO}$	0.0119	0.0030	0.0041
GEO1Post$_{NKN}$	0.0113	0.0029	0.0045
GEO1Post$_{PHO}$	0.0113	0.0029	0.0046
GEO2Pre$_{NKN}$	0.0123	0.0024	0.0043
GEO2Pre$_{PHO}$	0.0125	0.0026	0.0071
GEO2Post$_{NKN}$	0.0126	0.0028	0.0034
GEO2Post$_{PHO}$	0.0138	0.0017	0.0060
GEO3Pre$_{NKN}$	0.0085	0.0033	0.0105
GEO3Pre$_{PHO}$	0.0074	0.0044	0.0094
GEO3Post$_{NKN}$	0.0093	0.0042	0.0120
GEO3Post$_{PHO}$	0.0091	0.0042	0.0118
GEO4APre$_{NKN}$	0.0125	0.0062	0.0041
GEO4APre$_{PHO}$	0.0131	0.0059	0.0044
GEO4APost$_{NKN}$	0.0133	0.0079	0.0008
GEO4APost$_{PHO}$	0.0142	0.0065	0.0010
GEO4BPre$_{NKN}$	0.0126	0.0083	0.0008
GEO4BPre$_{PHO}$	0.0127	0.0083	0.0009
GEO4BPost$_{NKN}$	0.0129	0.0082	0.0006
GEO4BPost$_{PHO}$	0.0130	0.0083	0.0006
GEO4CPre$_{NKN}$	0.0127	0.0083	0.0016
GEO4CPre$_{PHO}$	0.0126	0.0083	0.0017
GEO4CPost$_{NKN}$	0.0128	0.0084	0.0011
GEO4CPost$_{PHO}$	0.0127	0.0084	0.0011
GEO4DPre$_{NKN}$	0.0128	0.0084	0.0011
GEO4DPre$_{PHO}$	0.0132	0.0085	0.0009
GEO4DPost$_{NKN}$	0.0132	0.0083	0.0011
GEO4DPost$_{PHO}$	0.0131	0.0085	0.0011

Fig. 8 shows the soil loss data, expressed in grams, derived from both the methodologies applied. For the surface elevation change-based method, the data coming from the DoDs obtained with both the Nikon and smartphone cameras are reported. From Fig. 8 emerges how the soil loss data estimated with the two methodologies are not comparable with each other, especially for the plots 1, 2, 3 and 4A, where only a single rainstorm was artificially reproduced. On the contrary, soil loss data derived from the same methodology, namely surface elevation change-based, are comparable with each other, independently from the type of camera used. Soil loss derived from the surface elevation change-based method result to be of two orders of magnitude greater than the one obtained with rainfall simulation. However, this discrepancy is in line with the processes that are involved and analysed with the two different methodologies. Rainfall simulation accounts for splash and initial inter-rill erosion processes and allows to study the impact of rain drops on sediment detachment, transport and runoff initiation. However, when it rains the water is able to disintegrate some of the soil aggregates, leading to the collapse of micro-pores and to the surface seal formation. Furthermore, the water that infiltrates makes also the soil heavier, causing a lowering of the soil surface, which is the process that DoDs are able to detect. To overcome this discrepancy between the two methodologies, sediment connectivity within the plots has been taken into consideration too.

3.3. Sediment connectivity analysis

Other than rainfall intensity and kinetic energy, also micro-topography plays a key role in the collection of eroded materials, especially when the experiments are carried out at very fine scales, as in our case. To prove this, Fig. 9 shows the maps of the connectivity index calculated with regard to the plots outlets, by considering, as inputs, the DEMsPre$_{NKN}$. As no reference theory exists for the partitioning of the connectivity index into classes, we relied on the same classification

Table 2

Accuracy measures of DEMs$_{PHO}$ checked by DEMs$_{NKN}$ with the assumption of normal distribution and more robust parameters too. DEMPre$_{NKN}$ and DEMPost$_{NKN}$ refer to DEMs derived from the Nikon camera before and after the rainfall simulation, respectively, and DEMPre$_{PHO}$ and DEMPost$_{PHO}$ for those derived from the smartphone camera before and after the rainfall simulation, respectively. The number of the plot is also included (1, 2, 3, 4A, 4B, 4C and 4D).

|	Minimum (m)	Maximum (m)	Mean (m)	SDE (m)	Kurtosis	Skeweness	NMAD (m)	Median (m)
DEM1Pre$_{PHO}$ - DEM1Pre$_{NKN}$	−0.0160	0.0210	0.0003	0.0022	12.5108	0.2772	0.0015	0.0003
DEM1Post$_{PHO}$ - DEM1Post$_{NKN}$	−0.0344	0.0336	−0.0002	0.0026	88.9927	−1.3843	0.0010	−0.0002
DEM2Pre$_{PHO}$ - DEM2Pre$_{NKN}$	−0.0135	0.0142	0.0015	0.0031	4.1464	−0.2322	0.0024	0.0017
DEM2Post$_{PHO}$ - DEM2Post$_{NKN}$	−0.0063	0.0173	0.0049	0.0029	3.9343	−0.0287	0.0022	0.0049
DEM3Pre$_{PHO}$ - DEM3Pre$_{NKN}$	−0.0062	0.0054	−0.0002	0.0019	2.5106	0.1547	0.0016	−0.0003
DEM3Post$_{PHO}$ - DEM3Post$_{NKN}$	−0.0056	0.0059	−0.0003	0.0010	6.3428	0.1691	0.0007	−0.0003
DEM4APre$_{PHO}$ - DEM4APre$_{NKN}$	−0.0139	0.0168	−0.0009	0.0026	8.5218	0.6003	0.0018	−0.0009
DEM4APost$_{PHO}$ - DEM4APost$_{NKN}$	−0.0201	0.0242	−0.0012	0.0043	5.6034	0.3439	0.0031	−0.0015
DEM4BPre$_{PHO}$ - DEM4BPre$_{NKN}$	−0.0193	0.0239	0.0003	0.0046	4.9291	0.0854	0.0034	0.0002
DEM4BPost$_{PHO}$ - DEM4BPost$_{NKN}$	−0.0067	0.0078	−0.0001	0.0014	6.2354	0.0027	0.0010	−0.0002
DEM4CPre$_{PHO}$ - DEM4CPre$_{NKN}$	−0.0057	0.0061	0.0001	0.0012	5.3686	−0.1376	0.0009	0.0002
DEM4CPost$_{PHO}$ - DEM4CPost$_{NKN}$	−0.0117	0.0128	0.0002	0.0028	5.6941	0.2353	0.0020	0.0002
DEM4DPre$_{PHO}$ - DEM4DPre$_{NKN}$	−0.0068	0.0092	−0.0001	0.0017	5.7170	0.5328	0.0012	−0.0002
DEM4DPost$_{PHO}$ - DEM4DPost$_{NKN}$	−0.0104	0.0115	0.0000	0.0023	5.8356	0.2322	0.0016	−0.0001

provided by Tarolli and Sofia (2016), in which they proposed to adopt a relative classification into four classes (High, Medium-High, Medium-Low and Low) by considering break points that best grouped similar values and maximized the differences between classes (natural breaks).

From Fig. 9 emerges how (i) each plot has different patterns of sediment connectivity, which vary whether or not consecutive rainstorms occur (Fig. 9d–g), and (ii) not all the soil within the plots is connected to the outlet. This proves the fact that the placement of the plots in the field is extremely important because micro-reliefs with their roughness can facilitate sediment dis-connectivity. The portions of soil that are more connected to the outlet are those that are closer to it. Therefore, these portions, which correspond to the Medium-High and High classes of the connectivity index maps, are reasonably those that will be more prone to erosion, once the rainstorm occurs. As a consequence, by masking the elevation differences maps (Fig. 7) with the Medium-High and High classes of the connectivity index maps (Fig. 9), we recomputed the soil loss derived from the surface elevation change-based method, considering both the Nikon (DoDs$_{NKN}$ IC) and smartphone (DoDs$_{PHO}$ IC) DoDs (Fig. 10).

Differently from what emerged from Fig. 8, Fig. 10 illustrates that the soil loss data, estimated with the two methodologies, are of the same order of magnitude, as long as the sediment connectivity within the plot is taken into consideration. These results confirm the importance of micro-topography in the sediment connectivity and, consequently, in the estimation of eroded materials.

4. Conclusions

In this work, we quantified the soil losses caused by water and compared them with each other, depending on two different methodologies applied: rainfall simulation and surface elevation change-based, relying on high-resolution DEMs derived from SfM. The experiments were carried out in a typical Mediterranean vineyard, under tillage conditions, at very fine scales. SfM data were derived from one standalone digital reflex camera and a smartphone built-in camera. We also applied an index of connectivity (IC) to evaluate the potential effect of sediment connectivity within the plots. Compared to the DEMs$_{NKN}$, we evaluated the DEMs$_{PHO}$ in terms of (i) accuracy, and (ii) capability to estimate soil
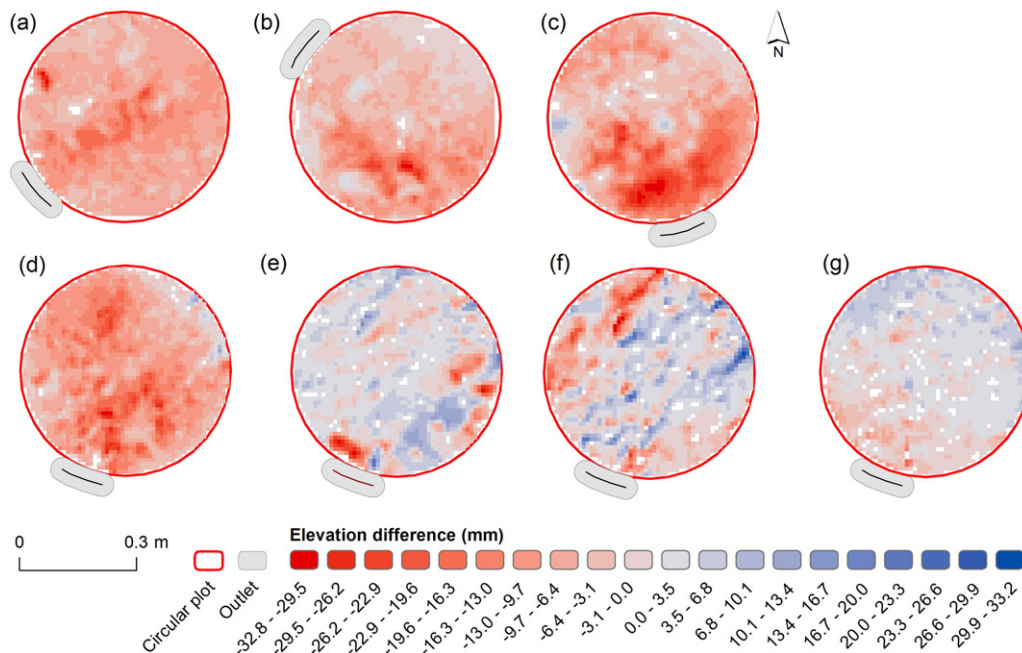
Fig. 7. DoDs derived from the Nikon dataset, thresholded according to the probabilistic thresholding with a 95% confidence interval and obtained for each plot: (a) Plot 1, (b) Plot 2, (c) Plot 3, (d) Plot 4A, (e) Plot 4B, (f) Plot 4C, and (g) Plot 4D.
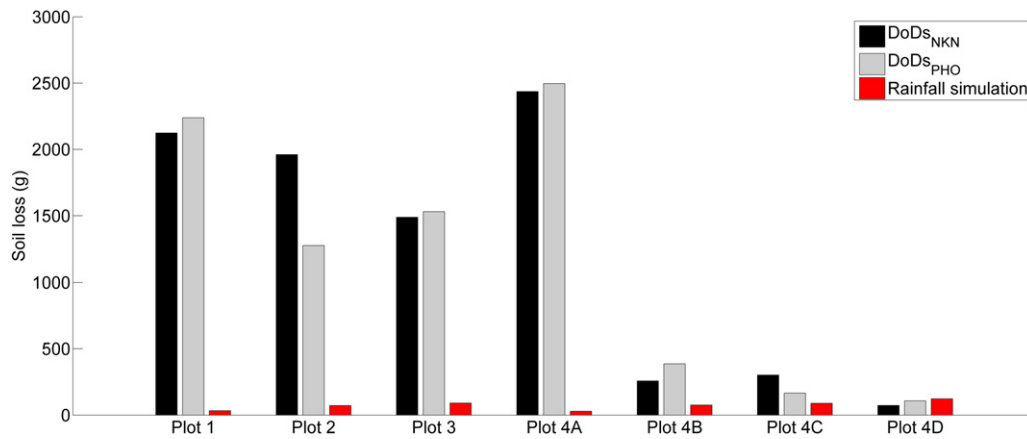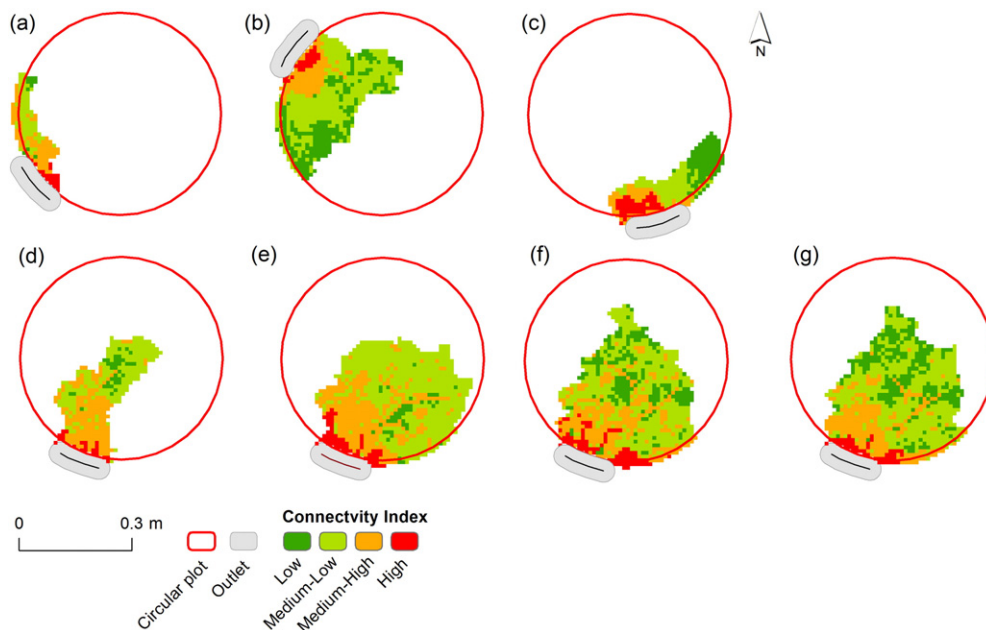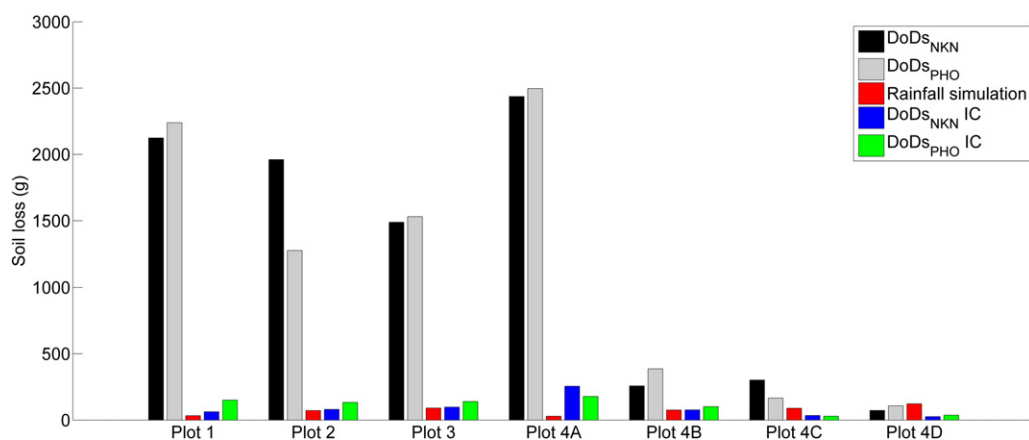
Fig. 8. Soil loss data, expressed in grams, derived for each plot from both the methodologies applied: rainfall simulation and surface elevation change-based relying on DoDs. $DoDs_{NKN}$ and $DoDs_{PHO}$ refer to soil loss estimated from Nikon and smartphone cameras, respectively.

loss with regard to the results derived from the rainfall simulation methodology. In terms of accuracy, the $DEMs_{PHO}$ revealed to be comparable with the $DEMs_{NKN}$, by assuming a normal distribution of errors and with more robust parameters too. Also regarding the estimation of soil losses, caused by the rainstorms artificially reproduced, through the surface elevation change-based methodology, the results between the two different types of cameras used were comparable with each other. What they differed from was the soil losses data estimated with the rainfall simulation. However, this discrepancy was overcome when the sediment connectivity within the plot was taken into consideration by computing the IC index. In conclusion, high-resolution topography derived from SfM revealed to be essential in the sediment connectivity analysis and, therefore, this, proved to play a key role in the estimation of eroded materials, if compared them to those derived from another methodology such as the rainfall simulation. SfM confirmed to be a useful approach to quantify topographic changes in agricultural lands, also at very fine scales, and revealed to be capable of detecting the more random changes, less easily traceable, induced by the rainstorms. In addition, the fact that smartphones built-in cameras

can produce as much satisfying results as those derived from standalone digital reflex cameras is undoubtedly a high value added. Nowadays, smartphones are commonly available for anyone, from farmers to researchers, and will become increasingly important for fast and cheap post-event analyses, as long as they are provided with a high-resolution camera. The increasing development of computer vision technologies and digital camera sensors makes the process of taking good pictures quite easy. A farmer would require few hours of training to learn how to take good pictures of a specific case study, i.e. a rill process, located in its own land. Afterwards, he would be completely independent during the whole field survey, and then he could send the pictures taken to a researcher for further analyses. In this way, the famer could easily keep monitoring some of the erosion processes that occur in his land and the researcher could provide him quantitative information about net erosion and deposition rates. However, it also should be said that the spatial scale plays a fundamental role in the feasibility of using smartphones for post-event analyses. For erosion processes that occur at field or catchment scales, the use of aerial photogrammetry, supported by the increasing diffusion of UAVs, is more recommended.

Fig. 9. Connectivity index maps calculated with regard to the plots outlets, by considering, as inputs, the $DEMsPre_{NKN}$, for each plot: (a) Plot 1, (b) Plot 2, (c) Plot 3, (d) Plot 4A, (e) Plot 4B, (f) Plot 4C, and (g) Plot 4D.

Fig. 10. Soil loss data, expressed in grams, derived for each plot from both the methodologies applied: rainfall simulation and surface elevation change-based relying on DoDs. DoDs$_{NKN}$ and DoDs$_{PHO}$ refer to soil loss estimated from Nikon and smartphone cameras, respectively. DoDs$_{NKN}$ IC and DoDs$_{PHO}$ IC refer to soil loss estimated from Nikon and smartphone cameras, respectively, by considering the connectivity index computed according to the DEMsPre.

References

Agisoft, 2016. Agisoft PhotoScan User Manual: Professional Edition. Version 1.0. http://www.agisoft.ru/products/photoscan/professional/ [September 2016].

Ali, G., Birkel, C., Tetzlaff, D., Soulsby, C., McDonnell, J.J., Tarolli, P., 2014. A comparison of wetness indices for the prediction of connected saturated areas under contrasted conditions. Earth Surf. Process. Landf. 39, 399–413.

Arnáez, J., Lasanta, T., Ruiz-Flaño, P., Ortigosa, L., 2007. Factors affecting runoff and erosion under simulated rainfall in Mediterranean vineyards. Soil Tillage Res. 93, 324–334.

Ashmore, P.E., Church, M., 1998. Sediment transport and river morphology: a paradigm for study. In: Klingeman, P.C., Beschta, R.L., Komar, P.D., Bradley, J.B. (Eds.), Gravelbed Rivers in the Environment. Water Resources Publications, Highlands Ranch, CO, pp. 115–148.

Aucelli, P.P.C., Conforti, M., Della Seta, M., Del Monte, M., D'uva, L., Rosskopf, C.M., Vergari, F., 2016. Multi-temporal digital photogrammetric analysis for quantitative assessment of soil erosion rates in the Landola catchment of the Upper Orcia Valley (Tuscany, Italy). Land Degrad. Dev. 27 (4), 1075–1092. http://dx.doi.org/10.1002/ldr.2324.

Baartman, J.E.M., Messelink, R., Keesstra, S.D., Temme, A.J.M., 2013. Linking landscape morphological complexity and sediment connectivity. Earth Surf. Process. Landf. 38, 1457–1471.

Bangen, S., Wheaton, J., Bouwes, N., Jordan, C., Volk, C., Ward, M.B., 2014. Crew variability in topographic surveys for monitoring wadeable streams: a case study from the Columbia River Basin. Earth Surf. Process. Landf. 39 (15), 2070–2086.

Bisantino, T., Bingner, R., Chouaib, W., Gentile, F., Trisorio Liuzzi, G., 2015. Estimation of runoff, peak discharge and sediment load at the event scale in a medium-size mediterranean watershed using the annagnps model. Land Degrad. Dev. 26 (4), 340–355. http://dx.doi.org/10.1002/ldr.2213.

Blavet, D., De Noni, G., Le Bissonnais, Y., Leonard, M., Maillo, L., Laurent, J.Y., Asseline, J., Leprun, J.C., Arshad, M.A., Roose, E., 2009. Effect of land use and management on the early stages of soil water erosion in French Mediterranean vineyards. Soil Tillage Res. 106, 124–136.

Borga, M., Anagnostou, E.N., Bloschl, G., Creutin, J.D., 2011. Flash flood forecasting, warning and risk management: the HYDRATE project. Environ. Sci. Pol. 14 (7), 834–844.

Borrelli, P., Märker, M., Schütt, B., 2015. Modelling post-tree-harvesting soil erosion and sediment deposition potential in the Turano river basin (Italian central Apennine). Land Degrad. Dev. 26 (4), 356–366. http://dx.doi.org/10.1002/ldr.2214.

Borselli, L., Cassi, P., Torri, D., 2008. Prolegomena to sediment and flow connectivity in the landscape: a GIS and field numerical assessment. Catena 75, 268–277.

Bracken, L.J., Croke, J., 2007. The concept of hydrological connectivity and its contribution to understanding runoff-dominated geomorphic systems. Hydrol. Process. 21, 1749–1763.

Bracken, J., Turnbull, L., Wainwright, J., Bogaart, P., 2015. Sediment connectivity: a framework for understanding sediment transfer at multiple scales. Earth Surf. Process. Landf. 40, 177–188.

Brasington, J., Rumsby, B.T., Mcvey, R.A., 2000. Monitoring and modelling morphological change in a braided gravel-bed river using high resolution GPS-based survey. Earth Surf. Process. Landf. 25 (9), 973–990.

Brasington, J., Langham, J., Rumsby, B., 2003. Methodological sensitivity of morphometric estimates of coarse fluvial sediment transport. Geomorphology 53 (3–4), 299–316.

Brierley, G., Fryirs, K., Jain, V., 2006. Landscape connectivity: the geographic basis of geomorphic applications. Area 38, 165–174.

Calligaro, S., Sofia, G., Prosdocimi, M., Dalla Fontana, G., Tarolli, P., 2013. Terrestrial laser scanner data to support coastal erosion analysis: the Conero case study. International Archives of the Photogrammetry, Remote Sensing and Spatial Information Sciences 40(5W3), pp. 125–129. http://dx.doi.org/10.5194/isprsarchives-XL-5-W3-125-2013.

Cao, L., Zhang, K., Dai, H., Liang, Y., 2015. Modeling interrill Erosion on Unpaved Roads in the Loess Plateau of China. Land Degrad. Dev. 26 (8), 825–832. http://dx.doi.org/10.1002/ldr.2253.

Cavalli, M., Trevisani, S., Comiti, F., Marchi, L., 2013. Geomorphometric assessment of spatial sediment connectivity in small alpine catchments. Geomorphology 188, 31–41.

Cerdà, A., 1996. Seasonal variability of infiltration rates under contrasting slope conditions in Southeast Spain. Geoderma 69, 217–232.

Cerdà, A., 1997. Soil erosion after land abandonment in a semiarid environment of southeastern Spain. Arid Soil Res. Rehabil. 11, 163–176.

Cerdà, A., 2000. Aggregate stability against water forces under different climates on agriculture land and scrubland in southern Bolivia. Soil Tillage Res. 57 (3), 159–166. http://dx.doi.org/10.1016/S0167-1987(00)00155-0.

Cerdà, A., Doerr, S.H., 2007. Soil wettability, runoff and erodibility of major dry-Mediterranean land use types on calcareous soils. Hydrol. Process. 21, 2325–2336. http://dx.doi.org/10.1016/j.catena.2008.03.010.

Cerdà, A., Ibàñez, S., Calvo, A., 1997. Design and operation of a small and portable rainfall simulator for rugged terrain. Soil Technol. 11, 161–170.

Cerdà, A., Flanagan, D.C., Le Bissonnais, Y., Boardman, J., 2009. Soil erosion and agriculture. Soil Tillage Res. 106, 107–108.

Cerdà, A., González-Pelayo, O., Giménez-Morera, A., Jordán, A., Pereira, P., Novara, A., Brevik, E.C., Prosdocimi, M., Mahmoodabadi, M., Keesstra, S., García Orenes, F., Ritsema, C., 2015. The use of barley straw residues to avoid high erosion and runoff rates on persimmon plantations in eastern Spain under low frequency - high magnitude simulated rainfall events. Soil Res. 54 (2), 154–165.

Cerdan, O., Govers, G., Le Bissonnais, Y., Van Oost, K., Poesen, J., Saby, N., Gobin, A., Vacca, A., Quinton, J., Auerwald, K., Klik, A., Kwaad, F.J.P.M., Raclot, D., Ionita, I., Rejman, J., Rousseva, S., Muxart, T., Roxo, M.J., Dostal, T., 2010. Rates and spatial variations of soil erosion in Europe: a study based on erosion plot data. Geomorphology 122, 167–177.

Chen, J., Li, K., Chang, K.-J., Sofia, G., Tarolli, P., 2015. Open-pit mining geomorphic feature characterisation. Int. J. Appl. Earth Obs. Geoinf. 42, 76–86.

Colomina, I., Molina, P., 2014. Unmanned aerial systems for photogrammetry and remote sensing: a review. ISPRS J. Photogramm. Remote Sens. 92, 79–97.

Costantini, E.A.C., Agnelli, A.E., Fabiani, A., Gagnarli, E., Mocali, S., Priori, S., Simoni, S., Valboa, G., 2015. Short-term recovery of soil physical, chemical, micro and mesobiological functions in a new vineyard under organic farming. Soil 1, 443–457. http://dx.doi.org/10.5194/soil-1-443-2015.

Dandois, J.P., Ellis, E.C., 2013. High spatial resolution three-dimensional mapping of vegetation spectral dynamics using computer vision. Remote Sens. Environ. 136, 259–276.

Doneus, M., Verhoeven, G., Fera, M., Briese, C., Kucera, M., Neubauer, W., 2011. From deposit to point cloud – a study of low cost computer vision approaches for the straightforward documentation of archeological excavations. Proceedings of the XXIIIrd International CIPA Symposium, Prague.

Eltner, A., Kaiser, A., Castillo, C., Rock, G., Neugirg, F., Abellán, A., 2015. Image-based surface reconstruction in geomorphometry – merits, limits and developments. Earth Surf. Dynam. 4, 359–389. http://dx.doi.org/10.5194/esurf-4-359-2016.

Fonstad, M.A., Dietrich, J.T., Courville, B.C., Jensen, J.L., Carbonneau, P.E., 2013. Topographic structure from motion: a new development in photogrammetric measurement. Earth Surf. Process. Landf. 38, 421–430.

Fryirs, K.A., Brierley, G.J., Preston, N.J., Kasai, M., 2007. Buffers, barriers and blankets: the (dis)connectivity of catchment-scale sediment cascades. Catena 70, 49–67.

Galati, A., Gristina, L., Crescimanno, M., Barone, E., Novara, A., 2015. Towards more efficient incentives for agri-environment measures in degraded and eroded vineyards. Land Degrad. Dev. 26, 557–564.

García-Ruiz, J.M., 2010. The effects of land uses on soil erosion in Spain: a review. Catena 81, 1–11.

García-Ruiz, J.M., Beguería, S., Nadal-Romero, E., Gonzalez-Hidalgo, J.C., Lana-Renault, N., Sansjuan, Y., 2015. A meta-analysis of soil erosion rates across the world. Geomorphology 239, 160–173.

Gessesse, B., Bewket, W., Bräuning, A., 2015. Model-based characterization and monitoring of runoff and soil erosion in response to land use/land cover changes in the Modjo Watershed, Ethiopia. Land Degrad. Dev. 26 (7), 711–724. http://dx.doi.org/10.1002/ldr.2276.

Giménez Morera, A., Ruiz Sinoga, J.D., Cerdà, A., 2010. The impact of cotton geotextiles on soil and water losses in Mediterranean rainfed agricultural land. Land Degrad. Dev. 21, 210–217.

Girardeau-Montaut, D., 2015. CloudCompare (Version 2.7) [GPL Software]. Retrieved from http://www.cloudcompare.org.

Grimaldi, S., Angelucccetti, I., Coviello, V., Vezza, P., 2015. Cost-effectiveness of soil and water conservation measures on the catchment sediment budget-the Laaba watershed case study, Burkina Faso. Land Degrad. Dev. 26 (7), 737–747. http://dx.doi.org/10.1002/ldr.2212.

Heckmann, T., Schwanghart, W., 2013. Geomorphic coupling and sediment connectivity in an alpine catchment – exploring sediment cascades using graph theory. Geomorphology 182, 89–103.

Höhle, J., Höhle, M., 2009. Accuracy assessment of digital elevation models by means of robust statistical methods. ISPRS J. Photogramm. Remote Sens. 64, 398–406.

Iserloh, T., Ries, J.B., Arnáez, J., Boix-Fayos, C., Butzen, V., Cerdà, A., Echeverría, M.T., Fernández-Gálvez, J., Fister, W., Geißler, C., Gómez, J.A., Gómez-Macpherson, H., Kuhn, N.J., Lázaro, R., León, F.J., Martínez-Mena, M., Martínez-Murillo, J.F., Marzen, M., Mingorance, M.D., Ortigosa, L., Peters, P., Regüés, D., Ruiz-Sinoga, J.D., Scholten, T., Seeger, M., Solé-Benet, A., Wengel, R., Wirtz, S., 2013. European small portable rainfall simulators: a comparison of rainfall characteristics. Catena 110, 100–112.

James, M.R., Robson, S., 2012. Straightforward reconstruction of 3D surfaces and topography with a camera: accuracy and geoscience application. J. Geophys. Res. 117, F03017.

Javernick, L., Brasington, B., Caruso, B., 2014. Modeling the topography of shallow braided rivers using structure-from-motion photogramnmetry. Geomorphology 213, 166–182.

Jordán, A., Zavala, L.M., Muñoz-Rojas, M., 2011. Mulching, effects on soil physical properties. In: Gliński, J., Horabik, J., Lipiec, J. (Eds.), Encyclopedia of Agrophysics. Springer, Dordrecht, pp. 492–496.

Keesstra, S., Pereira, P., Novara, A., Brevik, E.C., Azorin-Molina, C., Parras-Alcántara, L., Jordán, A., Cerdà, A., 2016. Effects of soil management techniques on soil water erosion in apricot orchards. Sci. Total Environ. 551-552, 357–366. http://dx.doi.org/10.1016/j.scitotenv.2016.01.182.

Lane, S.N., 1998. The use of digital terrain modelling in the understanding of dynamic river channel systems. In: Lane, S.N., Richards, K., Chandler, J. (Eds.), In Landform Monitoring, Modelling and Analysis. John Wiley & Sons, Chichester, pp. 311–342.

Lane, S.N., Chandler, J.H., Richards, K.S., 1994. Developments in monitoring and modeling small-scale river bed topography. Earth Surf. Process. Landf. 19 (4), 349–368. http://dx.doi.org/10.1002/esp.3290190406.

Lane, S.N., Westaway, R.M., Hicks, D.M., 2003. Estimation of erosion and deposition volumes in a large, gravel-bed, braided river using synoptic remote sensing. Earth Surf. Process. Landf. 28 (3), 249–271. http://dx.doi.org/10.1002/esp.483.

Lassu, T., Seeger, M., Peters, P., Keesstra, S.D., 2015. The Wageningen rainfall simulator: set-up and calibration of an indoor nozzle-type rainfall simulator for soil erosion studies. Land Degrad. Dev. 26 (6), 604–612. http://dx.doi.org/10.1002/ldr.2360.

León, J., Badía, D., Echeverría, M.T., 2015. Comparison of different methods to measure soil erosion in the central Ebro valley. Cuadernos De Investigacion Geografica 41 (1), 165–180. http://dx.doi.org/10.18172/cig.2703.

Lexartza-Artza, I., Wainwright, J., 2011. Making connections: changing sediment sources and sinks in an upland catchment. Earth Surf. Process. Landf. 36, 1090–1104.

Ligonja, P.J., Shrestha, R.P., 2015. Soil erosion assessment in Kondoa eroded area in Tanzania using universal soil loss equation, geographic information systems and socioeconomic approach. Land Degrad. Dev. 26 (4), 367–379. http://dx.doi.org/10.1002/ldr.2215.

López-Vicente, M., Poesen, J., Navas, A., Gaspar, L., 2013. Predicting runoff and sediment connectivity and soil erosion by water for different land use scenarios in the Spanish Pre-Pyrenees. Catena 102, 62–73.

López-Vicente, M., Quijano, L., Palazón, L., Gaspar, L., Navas, A., 2015. Assessment of soil redistribution at catchment scale by coupling a soil erosion model and a sediment connectivity index (Central Spanish Pre-Pyrenees). Cuadernos De Investigacion Geografica 41 (1), 127–147. http://dx.doi.org/10.18172/cig.2649.

López-Vicente, M., Nadal-Romero, E., Cammeraat, E.L.H., 2016. Hydrological connectivity does change over 70 years of abandonment and afforestation in the Spanish Pyrenees. Land Degrad. Dev. http://dx.doi.org/10.1002/ldr.2531.

Lowe, D., 2004. Distinctive image features from scale-invariant keypoints. Int. J. Comput. Vis. 60, 91–110.

Marchamalo, M., Hooke, J.M., Sandercock, P.J., 2016. Flow and sediment connectivity in semi-arid landscapes in SE Spain: patterns and controls. Land Degrad. Dev. 27 (4), 1032–1044. http://dx.doi.org/10.1002/ldr.2352.

Martínez-Casasnovas, J.A., Sánchez-Bosch, I., 2000. Impact assessment of changes in land use/conservation practices on soil erosion in the Penedès-Anoia vineyard region (NE Spain). Soil Tillage Res. 57, 101–106.

Martínez-Casasnovas, J.A., Ramos, M.C., Ribes-Dasi, M., 2002. Soil erosion caused by extreme rainfall events: mapping and quantification in agricultural plots from very detailed digital elevation models. Geoderma 105, 125–140.

Masiero, A., Vettore, A., 2016. Improved feature matching for mobile devices with IMU. Sensors 16, 1243. http://dx.doi.org/10.3390/s16081243.

Masiero, A., Guarnieri, A., Pirotti, F., Vettore, A., 2015. Semi-automated detection of surface degradation on bridges based on a level set method. Int. Arch. Photogramm. Remote. Sens. Spat. Inf. Sci. 15–21. http://dx.doi.org/10.5194/isprsarchives-XL-3-W3-15-2015 XL-3/W3.

Masselink, R.J.H., Keesstra, S.D., Temme, A.J.A.M., Seeger, M., Giménez, R., Casalí, J., 2016. Modelling discharge and sediment yield at catchment scale using connectivity components. Land Degrad. Dev. 27 (4), 933–945. http://dx.doi.org/10.1002/ldr.2512.

Mekonnen, M., Keesstra, S.D., Baartman, J.E., Ritsema, C.J., Melesse, A.M., 2015a. Evaluating sediment storage dams: structural off-site sediment trapping measures in northwest Ethiopia. Cuadernos De Investigacion Geografica 41 (1), 7–22. http://dx.doi.org/10.18172/cig.2643.

Mekonnen, M., Keesstra, S.D., Stroosnijder, L., Baartman, J.E.M., Maroulis, J., 2015b. Soil conservation through sediment trapping: a review. Land Degrad. Dev. 26 (6), 544–556. http://dx.doi.org/10.1002/ldr.2308.

Mekuria, W., Langan, S., Noble, A., Johnston, R., 2016. Soil restoration after seven years of exclosure management in northwestern Ethiopia. Land Degrad. Dev. http://dx.doi.org/10.1002/ldr.2527.

Mengistu, D., Bewket, W., Lal, R., 2016. Conservation effects on soil quality and climate change adaptability of Ethiopian watersheds. Land Degrad. Dev. 27 (6), 1603–1621. http://dx.doi.org/10.1002/ldr.2376.

Micheletti, N., Chandler, J.H., Lane, S.N., 2014. Investigating the geomorphological potential of freely available and accessible structure-from-motion photogrammetry using a smartphone. Earth Surf. Process. Landf. 40 (4), 473–486. http://dx.doi.org/10.1002/esp.3648.

Montgomery, D.R., 2007. Soil erosion and agricultural sustainability. PNAS 104, 13268–13272.

Mwango, S.B., Msanya, B.M., Mtakwa, P.W., Kimaro, D.N., Deckers, J., Poesen, J., 2016. Effectiveness of mulching under miraba in controlling soil erosion, fertility restoration and crop yield in the Usambara Mountains, Tanzania. Land Degrad. Dev. 27 (4), 1266–1275. http://dx.doi.org/10.1002/ldr.2332.

Nanko, K., Giambelluca, T.W., Sutherland, R.A., Mudd, R.G., Nullet, M.A., Ziegler, A.D., 2015. Erosion potential under Miconia calvescens stands on the island of Hawai'i. Land Degrad. Dev. 26, 218–226. http://dx.doi.org/10.1002/ldr.2200.

Novara, A., Gristina, L., Saladino, S.S., Santoro, A., Cerdà, A., 2011. Soil erosion assessment on tillage and alternative soil managements in a Sicilian vineyard. Soil Tillage Res. 117, 140–147.

Novara, A., Keesstra, S., Cerdà, A., Pereira, P., Gristina, L., 2016. Understanding the role of soil erosion on co_2-c loss using ^{13}c isotopic signatures in abandoned Mediterranean agricultural land. Sci. Total Environ. 550, 330–336. http://dx.doi.org/10.1016/j.scitotenv.2016.01.095.

Ochoa-Cueva, P., Fries, A., Montesinos, P., Rodríguez-Díaz, J.A., Boll, J., 2015. Spatial estimation of soil erosion risk by land-cover change in the Andes of Southern Ecuador. Land Degrad. Dev. 26 (6), 565–573. http://dx.doi.org/10.1002/ldr.2219.

Piermattei, L., Carturan, L., de Blasi, F., Tarolli, P., Dalla Fontana, G., Vettore, A., Pfeifer, N., 2016. Suitability of ground-based SfM–MVS for monitoring glacial and periglacial processes. Earth Surf. Dyn. 4, 425–443.

Prosdocimi, M., Calligaro, S., Sofia, G., Dalla Fontana, G., Tarolli, P., 2015. Bank erosion in agricultural drainage networks: new challenges from structure-from-motion photogrammetry for post-event analysis. Earth Surf. Process. Landf. 40, 1891–1906.

Prosdocimi, M., Cerdà, A., Tarolli, P., 2016a. Soil water erosion on Mediterranean vineyards: a review. Catena 141, 1–21.

Prosdocimi, M., Jordán, A., Tarolli, P., Keesstra, S., Novara, A., Cerdà, A., 2016b. The immediate effectiveness of barley straw mulch in reducing soil erodibility and surface runoff generation in Mediterranean vineyards. Sci. Total Environ. 547, 323–330.

Prosdocimi, M., Tarolli, P., Cerdà, A., 2016c. Mulching practices for reducing soil water erosion: A review. Earth Sci. Rev. 161, 191–203. http://dx.doi.org/10.1016/j.earscirev.2016.08.006.

Raclot, D., Le Bissonnais, Y., Louchart, X., Andrieux, P., Moussa, R., Voltz, M., 2009. Soil tillage and scale effects on erosion from fields to catchment in a Mediterranean vineyard area. Agric. Ecosyst. Environ. 134, 201–210.

Reid, S.C., Lane, S.N., Montgomery, D.R., Brookes, C.J., 2007. Does hydrological connectivity improve modelling of coarse sediment delivery in upland environments? Geomorphology 90, 263–282.

Robertson, D.P., Cipolla, R., 2009. Structure from motion. In: Varga, M. (Ed.), Practical Image Processing and Computer Vision. John Wiley & Sons, Chichester.

Rodrigo Comino, J., Brings, C., Lassu, T., Iserloh, T., Senciales, J.M., Martínez Murillo, J.F., Ruiz Sinoga, J.D., Seeger, M., Ries, J.B., 2015. Rainfall and human activity impacts on soil losses and rill erosion in vineyards (Ruwer Valley, Germany). Solid Earth 6, 823–837. http://dx.doi.org/10.5194/se-6-823-2015.

Rodrigo Comino, J., Iserloh, T., Lassu, T., Cerdà, A., Keesstra, S.D., Prosdocimi, M., Brings, C., Marzen, M., Ramos, M.C., Senciales, J.M., Ruiz Sinoga, J.D., Seeger, M., Ries, J.B., 2016a. Quantitative comparison of initial soil erosion processes and runoff generation in Spanish and German vineyards. Sci. Total Environ. 565, 1165–1174. http://dx.doi.org/10.1016/j.scitotenv.2016.05.163.

Rodrigo Comino, J., Iserloh, T., Morvan, X., Malam Issa, O., Naisse, C., Keesstra, S., Cerdà, A., Prosdocimi, M., Arnáez, J., Lasanta, T., Ramos, M.C., Marqués, M.J., Ruiz Colmenero, M., Bienes, R., Ruiz Sinoga, J.D., Seeger, M., Ries, J.B., 2016b. Soil erosion processes in European vineyards: a qualitative comparison of rainfall simulation measurements in Germany, Spain and France. Hydrology 3 (6). http://dx.doi.org/10.3390/hydrology3010006.

Rodrigo Comino, J., Seeger, M., Senciales, J.M., Ruiz-Sinoga, J.D., Ries, J.B., 2016c. Spatial and temporal variation of soil hydrological processes on steep slope vineyards

(Ruwel-Mosel Valley, Gemany). Cuadernos De Investigacion Geografica 42 (1), 281–306. http://dx.doi.org/10.18172/cig.2934.

Sibson, R., 1981. A brief description of natural neighbor interpolation. In: Barnett, V. (Ed.), Interpreting Multivariate Data. John Wiley & Sons, Chichester, pp. 21–36 chapter 2.

Sofia, G., Pirotti, F., Tarolli, P., 2013. Variations in multiscale curvature distribution and signatures of lidar DEM errors. Earth Surf. Process. Landf. 38, 1116–1134.

Sofia, G., Hillier, J.K., Conway, S.J., 2016. Frontiers in geomorphometry and earth surface dynamics: possibilities, limitations and perspectives. Earth Surf. Dynam. 4, 1–5. http://dx.doi.org/10.5194/esurf-4-1-2016.

Soil Survey Staff, 1998. Keys of Soil Taxonomy. 8th ed. USDA-NRCS, Washington DC.

Sougnez, N., Van Wesemael, B., Vanacker, V., 2011. Low erosion rates measured for steep, sparsely vegetated catchments in southeast Spain. Catena 84, 1–11.

Taguas, E.V., Guzmán, E., Guzmán, G., Vanwalleghem, T., Gómez, J.A., 2015. Characteristics and importance of rill and gully erosion: a case study in a small catchment of a marginal olive grove. Cuadernos De Investigacion Geografica 41 (1), 107–126. http://dx.doi.org/10.18172/cig.2644.

Tarboton, D.G., 2013. Taudem 5.1, Terrain Analysis Using Digital Elevation Models [Online]. Available from http://hydrology.usu.edu/taudem/taudem5/.

Tarolli, P., 2014. High-resolution topography for understanding earth surface processes: opportunities and challenges. Geomorphology 216, 295–312.

Tarolli, P., Sofia, G., 2016. Human topographic signatures and derived geomorphic processes across landscapes. Geomorphology 255, 140–161.

Tarolli, P., Preti, F., Romano, N., 2014. Terraced landscapes: from an old best practice to a potential hazard for soil degradation due to land abandonment. Anthropocene 6, 10–25.

Tarolli, P., Sofia, G., Calligaro, S., Prosdocimi, M., Preti, F., Dalla Fontana, G., 2015. Vineyards in terraced landscapes: new opportunities from lidar data. Land Degrad. Dev. 26, 92–102.

Taylor, J., 1997. An Introduction to Error Analysis: The Study of Uncertainties in Physical Measurements. 2nd edn. Sausalito, CA, University Science Books.

Theler, D., Reynard, E., Lambiel, C., Bardou, E., 2010. The contribution of geomorphological mapping to sediment transfer evaluation in small alpine catchments. Geomorphology 124, 113–123.

Verhoeven, G., Doneus, M., Briese, C., Vermeulen, F., 2012. Mapping by matching: a computer vision-based approach to fast and accurate georeferencing of archaeological aerial photographs. J. Archaeol. Sci. 39, 2060–2070.

Wainwright, J., Turnbull, L, Ibrahim, T.G., Lexartza-Artza, I., Thornton, S.F., Brazier, R.E., 2011. Linking environmental regimes, space and time: interpretations of structural and functional connectivity. Geomorphology 126, 387–404.

Walter, H., Lieth, H., 1960. Klimadiagramma-Weltatlas. G. Fischer Verlag, Jena.

Wechsler, S.P., 2007. Uncertainties associated with digital elevation models for hydrologic applications: a review. Hydrol. Earth Syst. Sci. 11, 1481–1500.

Westoby, M.J., Brasington, J., Glasser, N.F., Hambrey, M.J., Reynolds, J.M., 2012. 'Structure-from-Motion' photogrammetry: a low-cost, effective tool for geosciences applications. Geomorphology 17, 300–314.

Wheaton, J.M., 2008. Uncertainty in Morphological Sediment Budgeting of Rivers, Unpublished PhD thesis. University of Southampton 412 pp http://www.joewheaton.org/Home/research/projects-1/morphological-sediment-budgeting/phdthesis.

Wheaton, J.M., Brasington, J., Darby, S.E., Sear, D.A., 2010. Accounting for uncertainty in DEMs from repeat topographic surveys: improved sediment budgets. Earth Surf. Process. Landf. 35, 136–156.

Whitehead, K., Moorman, B.J., Hugenholtz, C.H., 2013. Brief communication: low-cost, on-demand aerial photogrammetry for glaciological measurement. Cryosphere 7, 1879–1884.

Woodget, A.S., Carbonneau, P.E., Visser, F., Maddock, I., 2015. Quantifying submerged fluvial topography using hyperspatial resolution UAS imagery and structure from motion photogrammetry. Earth Surf. Process. Landf. 40, 47–64. http://dx.doi.org/10.1002/esp.3613.